Supplement of Atmos. Chem. Phys., 20, 14917–14932, 2020
https://doi.org/10.5194/acp-20-14917-2020-supplement

Supplement of

Elevated dust layers inhibit dissipation of heavy anthropogenic surface air pollution

Zhuang Wang et al.

Correspondence to: Cheng Liu (chliu81@ustc.edu.cn), Zhouqing Xie (zqxie@ustc.edu.cn) and Qihou Hu (qhhu@aiofm.ac.cn)

Section S1. Inversion method and data verification of RL parameters

Lidar ratio (LR) at 355 nm. Aerosol LR ($S_{\lambda_o}^{aer}$) is defined as the aerosol extinction–to–backscatter ratio ($S_{\lambda_o}^{aer}(z_o)=\alpha_{\lambda_o}^{aer}(z_o)/\beta_{\lambda_o}^{aer}(z_o)$). The aerosol extinction coefficients ($\alpha_{\lambda_o}^{aer}$) and backscatter coefficients ($\beta_{\lambda_o}^{aer}$) at 355 nm were calculated from the elastic and inelastic return signals (Ansmann et al., 1990; Ansmann et al., 1992b). We assumed particle scattering to be proportional to λ^{-k} with the value of k=1 for pollution aerosol (Ansmann et al., 2005) and k=0 for dust (Ansmann et al., 1992a). The nitrogen molecule number density, atmospheric molecule extinction, and atmospheric molecule backscatter were derived from a standard atmosphere model. Only nighttime (from 18:00 to 06:00 local time) data were used to compute the LR due to the large daytime background noise. Moreover, 10–point spatial smoothing and three–hour averaging for the nitrogen Raman signal were used to reduce the relative error in computing the LR (Fig. S12). The overlap function (Wandinger and Ansmann, 2002) must be used to determine the LR in the lower lidar layer, it was computed under clear conditions.

Particle linear depolarization ratio (PLDR) at 532 nm. Volume linear depolarization ratio (VLDR) is calculated from the ratio of the calibrated perpendicular polarized signal to the parallel polarized signal, and then PLDR is derived from VLDR and backscatter coefficient (Freudenthaler et al., 2009).

Aerosol extinction coefficient at 355 nm (EXT_{355}). As the signal–to–noise ratio of the inelastic backscatter Raman signal was extremely low during daytime, only the elastic backscatter signal was available and thus the Fernald method (Klett, 1981; Fernald, 1984) had to be used to retrieve the EXT_{355}. This method requires two crucial assumptions, a reference value of the EXT_{355} as in the inelastic method and the range–dependent LR, which may cause greater errors under heavy pollution conditions (Sasano et al., 1985). To obtain accurate values of the EXT_{355}, a reasonable evaluation of the range–dependent LR is necessary. Considering that the vertical structure of aerosols in the same heavy pollution incident has similar characteristics, we used the nighttime average LR to represent the daytime values. In addition, a 10–point spatial smoothing average for the elastic backscatter signal was used to reduce the relative error in computing the EXT_{355}.

Aerosol extinction coefficient at 532 nm (EXT_{532}). The total elastic backscatter signal (Ansmann et al., 1992a) profile at 532 nm was used to compute the EXT_{532}, which is defined as $P_{532}(z)=P_{532p}(z)+P_{532s}(z)$. The retrieval method is the same as that using the elastic backscatter signal to compute the EXT_{355}, but the LR at 355 nm was set equal to the LR at 532 nm (Sugimoto et al., 2002). This assumption may introduce additional errors due to the wavelength dependence of LR (Groß et al., 2015; Groß et al., 2017). Thus, the EXT_{355} was used to analyze the air pollution status during the observation period.

Water vapor mixing ratio. The water vapor mixing ratio can be defined as the ratio of water vapor mass to the dry air mass within a certain volume. The water vapor mixing ratio m(z) can be derived by detecting the Raman signal of water vapor (Whiteman et al., 1992; Behrendt et al., 2002)

$$m(z)=c_m*\Delta q_m(z_0,z)*\frac{I_H(z)}{I_Z(z)} \quad (1)$$

Where z is the height; c_m is the system calibration constant; Δq_m is the transmission correction function; and I_H and I_N are the inelastic backscatter Raman signals of water vapor and nitrogen, respectively. A 10–point spatial smoothing and hourly average for the water vapor and nitrogen Raman signal were used to calculate the water mixing ratio to reduce relative error. Relative humidity (RH) can be obtained by combining the water vapor mixing ratio m(z) measured by RL and the temperature and pressure profile simulated by the Weather Research and Forecasting (WRF) model coupled with Chemistry (WRF–Chem) model. We needed to spline–interpolate the spatial resolution of temperature and pressure profile to 7.5 m due to the different spatial resolution between WRF–Chem model and RL.

In addition, the seasonal average vertical structure of EXT_{532} and PLDR was compared with the Cloud–Aerosol Lidar and Infrared Pathfinder Satellite Observations (CALIPSO) lidar. The CALIPSO satellite provides the vertical structure of global aerosols since Jun 2006. The system emits linearly polarized light at 532 and 1064 nm, and simultaneously receives 532 nm parallel and cross–polarized backscatter signals. A complete overview of the architecture and performance of CALIPSO and the data retrieval algorithms can be found in Hunt et al., 2009 and Winker et al., 2009, respectively. The CALIPSO level 2 aerosol profile products ("CAL_LID_L2_05kmAPro–Prov–V3–40"), including EXT_{532} nm and PLDR at 532 nm, are used for comparison. It is difficult to expect aerosols in the planetary boundary layer to be similarly distributed over a long distances (Anderson et al., 2003). Thus, only CALIPSO overpasses that occurred at a distance of less than 150 km and a temporal difference of less than 1h were selected. A total number of 18 overpasses from 23 Jan to 29 Mar 2017 was found, 15 qualified for comparison. Details of the 15 cases used for comparison are listed in Table S2. Figure S13 provides a comparison of three–month average aerosol extinction coefficient and PLDR vertical structure between RL and CALIPSO satellite measurements. We also calculated the relative bias to quantify the comparison by the following equation:

$$\text{Bias}(z)=100\%*\frac{\delta_{CALIPSO}(z)\text{-}\delta_{RL}(z)}{\delta_{CALIPSO}(z)} \quad (2)$$

Where z is the height, δ is the EXT_{532} or depolarization ratio measured by RL and CALIPSO. Generally, the three–month average comparison results are in reasonable agreement with such efforts over other parts of the world (Pappalardo et al., 2010; Tesche et al., 2013).

References

Anderson, T. L., Charlson, R. J., Winker, D. M., Ogren, J. A., and Holmén, K.: Mesoscale variations of tropospheric aerosols, J. Atmos. Sci., 60, 119-136, doi: 10.1175/1520-0469(2003)060<0119:MVOTA>2.0.CO;2, 2003.

Ansmann, A., Engelmann, R., Althausen, D., Wandinger, U., Hu, M., Zhang, Y., He, Q.: High aerosol load over the Pearl River Delta, China, observed with Raman lidar and Sun photometer, Geophys. Res. Lett., 32, L13815, doi: 10.1029/2005gl023094, 2005.

Ansmann, A., Riebesell, M., and Weitkamp, C.: Measurement of atmospheric aerosol extinction profiles with a Raman lidar, Opt. Lett., 15, 746-748, doi: 10.1364/OL.15.000746, 1990.

Ansmann, A., Riebesell, M., Wandinger, U., Weitkamp, C., Voss, E., Lahmann, W., and Michaelis, W.: Combined Raman elastic-backscatter lidar for vertical profiling of moisture, aerosol extinction, backscatter, and lidar ratio, Appl. Phys. B, 55, 18-28, 1992a.

Ansmann, A., Wandinger, U., Riebesell, M., Weitkamp, C., and Michaelis, W.: Independent measurement of extinction and backscatter profiles in cirrus clouds by using a combined Raman elastic-backscatter lidar, Appl. Opt., 31, 7113-7131, doi: 10.1364/AO.31.007113, 1992b.

Behrendt, A., Nakamura, T., Onishi, M., Baumgart, R., and Tsuda, T.: Combined Raman lidar for the measurement of atmospheric temperature, water vapor, particle extinction coefficient, and particle backscatter coefficient, Appl. Opt., 41, 7657-7666, doi: 10.1364/AO.41.007657, 2002.

Fernald, F. G.: Analysis of atmospheric lidar observations: some comments, Appl. Opt., 23, 652-653, doi: 10.1364/AO.23.000652, 1984.

Freudenthaler, V., Esselborn, M., Wiegner, M., Heese, B., Tesche, M., Ansmann, A., MüLler, D., Althausen, D., Wirth, M., Fix, A., Ehret, G., Knippertz, P., Toledano, C., Gasteiger, J., Garhammer, M., and Seefeldner, M.: Depolarization ratio profiling at several wavelengths in pure Saharan dust during SAMUM 2006, Tellus B, 61, 165-179, doi: 10.1111/j.1600-0889.2008.00396.x, 2009.

Groß, S., Freudenthaler, V., Wirth, M., and Weinzierl, B.: Towards an aerosol classification scheme for future EarthCARE lidar observations and implications for research needs, Atmos. Sci. Lett., 16, 77-82, doi: 10.1002/asl2.524, 2015.

Groß, S., Tesche, M., Freudenthaler, V., Toledano, C., Wiegner, M., Ansmann, A., Althausen, D., and Seefeldner, M.: Characterization of Saharan dust, marine aerosols and mixtures of biomass-burning aerosols and dust by means of multi-wavelength depolarization and Raman lidar measurements during SAMUM 2, Tellus B, 63, 706-724, doi: 10.1111/j.1600-0889.2011.00556.x, 2017.

Heese, B., Flentje, H., Althausen, D., Ansmann, A., and Frey, S.: Ceilometer lidar comparison: backscatter coefficient retrieval and signal-to-noise ratio determination, Atmos. Meas. Tech., 3, 1763-1770, doi: 10.5194/amt-3-1763-2010, 2010.

Hunt, W. H., Winker, D. M., Vaughan, M. A., Powell, K. A., Lucker, P. L., and Weimer, C.: CALIPSO Lidar Description and Performance Assessment, J. Atmos. Oceanic Technol., 26, 1214-1228, doi: 10.1175/2009jtecha1223.1, 2009.

Klett, J. D.: Stable analytical inversion solution for processing lidar returns, Appl. Opt., 20, 211-220, doi: 10.1364/AO.20.000211, 1981.

Murayama, T., Okamoto, H., Kaneyasu, N., Kamataki, H., and Miura, K.: Application of lidar depolarization measurement in the atmospheric boundary layer: Effects of dust and sea-salt particles, J. Geophys. Res. Atmos., 104, 31781-31792, doi: 10.1029/1999jd900503, 1999.

Pappalardo, G., Wandinger, U., Mona, L., Hiebsch, A., Mattis, I., Amodeo, A., Ansmann, A., Seifert, P., Linné, H., Apituley, A., Alados Arboledas, L., Balis, D., Chaikovsky, A., D'Amico, G., De Tomasi, F., Freudenthaler, V., Giannakaki, E., Giunta, A., Grigorov, I., Iarlori, M., Madonna, F., Mamouri, R.-E., Nasti, L., Papayannis, A., Pietruczuk, A., Pujadas, M., Rizi, V., Rocadenbosch, F., Russo, F., Schnell, F., Spinelli, N., Wang, X., and Wiegner, M.: EARLINET correlative measurements for CALIPSO: First intercomparison results, J. Geophys. Res., 115, D00H19, doi: 10.1029/2009jd012147, 2010.

Sasano, Y., Browell, E. V., and Ismail, S.: Error caused by using a constant extinction/backscattering ratio in the lidar solution, Appl. Opt, 24, 3929, doi: 10.1364/ao.24.003929, 1985.

Sugimoto, N., Matsui, I., Shimizu, A., Uno, I., Asai, K., Endoh, T., and Nakajima, T.: Observation of dust and anthropogenic aerosol plumes in the Northwest Pacific with a two-wavelength polarization lidar on board the research vessel Mirai, Geophys. Res. Lett., 29, 1901, doi: 10.1029/2002gl015112, 2002.

Tesche, M., Wandinger, U., Ansmann, A., Althausen, D., Müller, D., and Omar, A. H.: Ground-based validation of CALIPSO observations of dust and smoke in the Cape Verde region, J. Geophys. Res. Atmos., 118, 2889-2902, doi: 10.1002/jgrd.50248, 2013.

Wandinger, U., and Ansmann, A.: Experimental determination of the lidar overlap profile with Raman lidar, Appl. Opt., 41, 511-514, doi: 10.1364/AO.41.000511, 2002.

Whiteman, D., Melfi, S., and Ferrare, R.: Raman lidar system for the measurement of water vapor and aerosols in the Earth's atmosphere, Appl. Opt., 31, 3068-3082, doi: 10.1364/AO.31.003068, 1992.

Winker, D. M., Vaughan, M. A., Omar, A., Hu, Y., Powell, K. A., Liu, Z., Hunt, W. H., and Young, S. A.: Overview of the CALIPSO Mission and CALIOP Data Processing Algorithms, J. Atmos. Oceanic Technol., 26, 2310-2323, doi: 10.1175/2009jtecha1281.1, 2009.

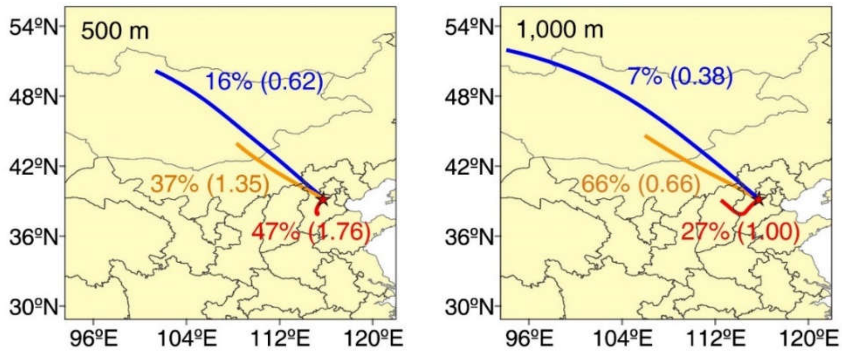

Figure S1. Cluster analysis of 24–h air mass backward trajectories (AMBTs) initialized at 500 m and 1000 m from 20 Jan to 5 Feb 2017. The numbers in the map are the fraction of each category of AMBTs and the numbers in brackets are the corresponding spatially average EXT_{355} value at 450 m–550 m and 950 m–1050 m (unit: km^{-1}), respectively. The 24–hour AMBTs were computed using the Hybrid Single–Particle Lagrangian Integrated Trajectory (HYSPLIT) model of the National Oceanic and Atmospheric Administration (Draxler and Hess, 1998). We calculated the hourly AMBTs during the whole observation period initialized at 500 m and 1000 m. Then, cluster analysis of AMBTs was conducted in three categories directions. Base map is from TrajStat 1.2.2 software (http://www.meteothinker.com).

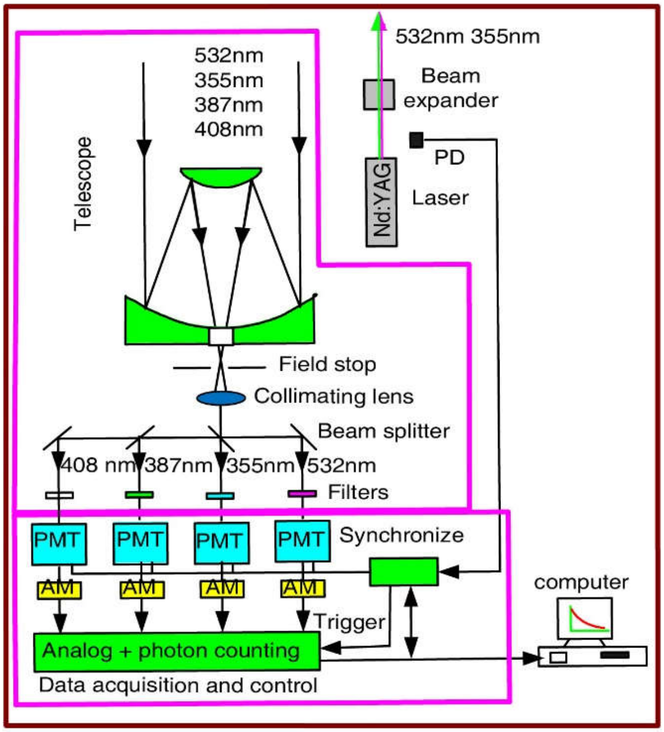

Figure S2. Schematic of multi–wavelength polarization RL system.

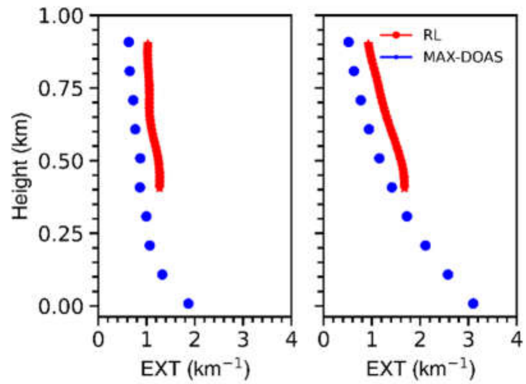

Figure S3. Comparison of average EXT profile during HPI 1 (left) and HPI 2 (right) between RL and MAX–DOAS.

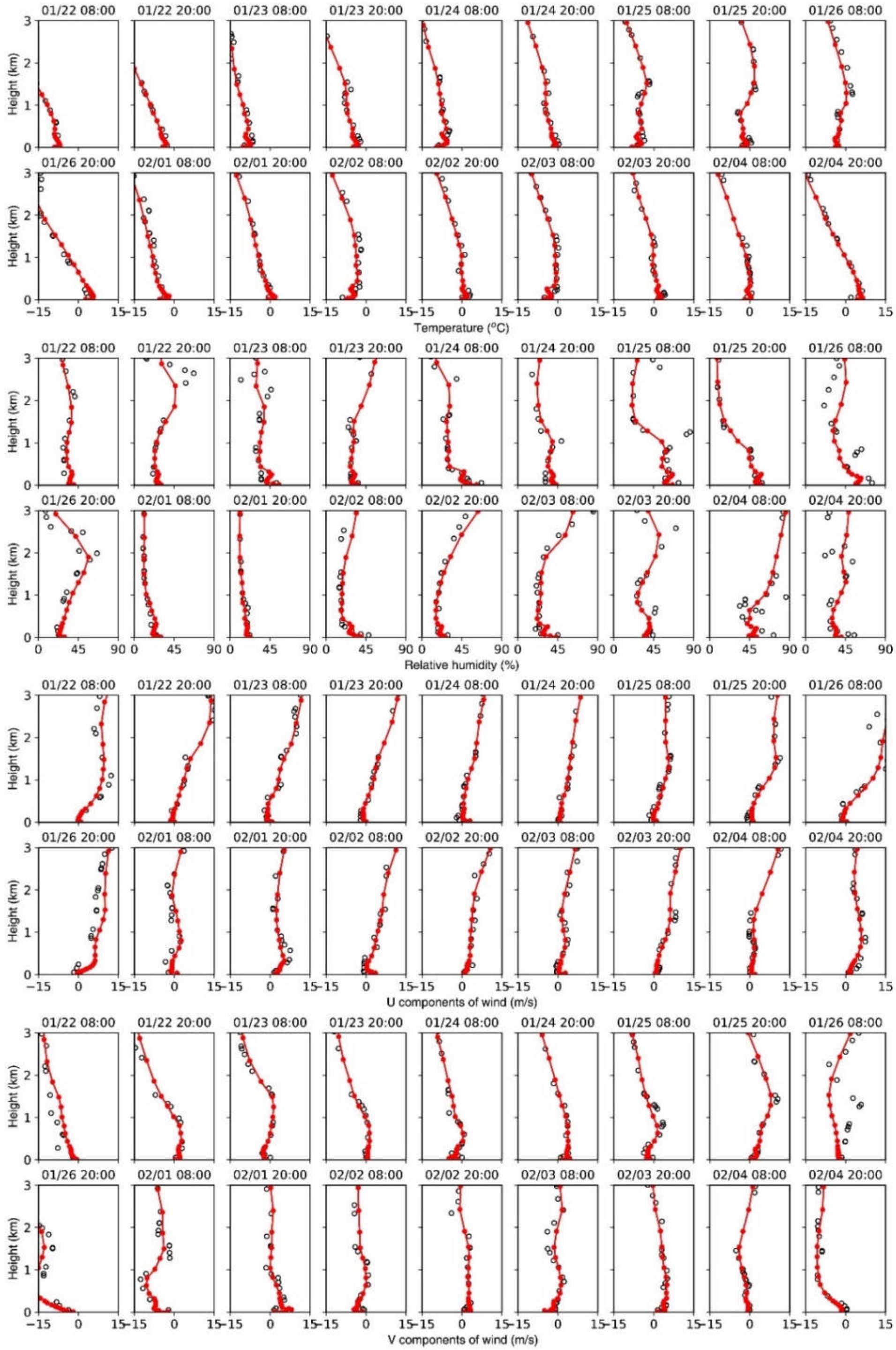

Figure S4. Comparison of the vertical profiles of temperature, vertical profiles of relative humidity, vertical profiles of wind speed (u components), and vertical profiles of wind speed (v components) between simulations (red dots) and observations (black dots).

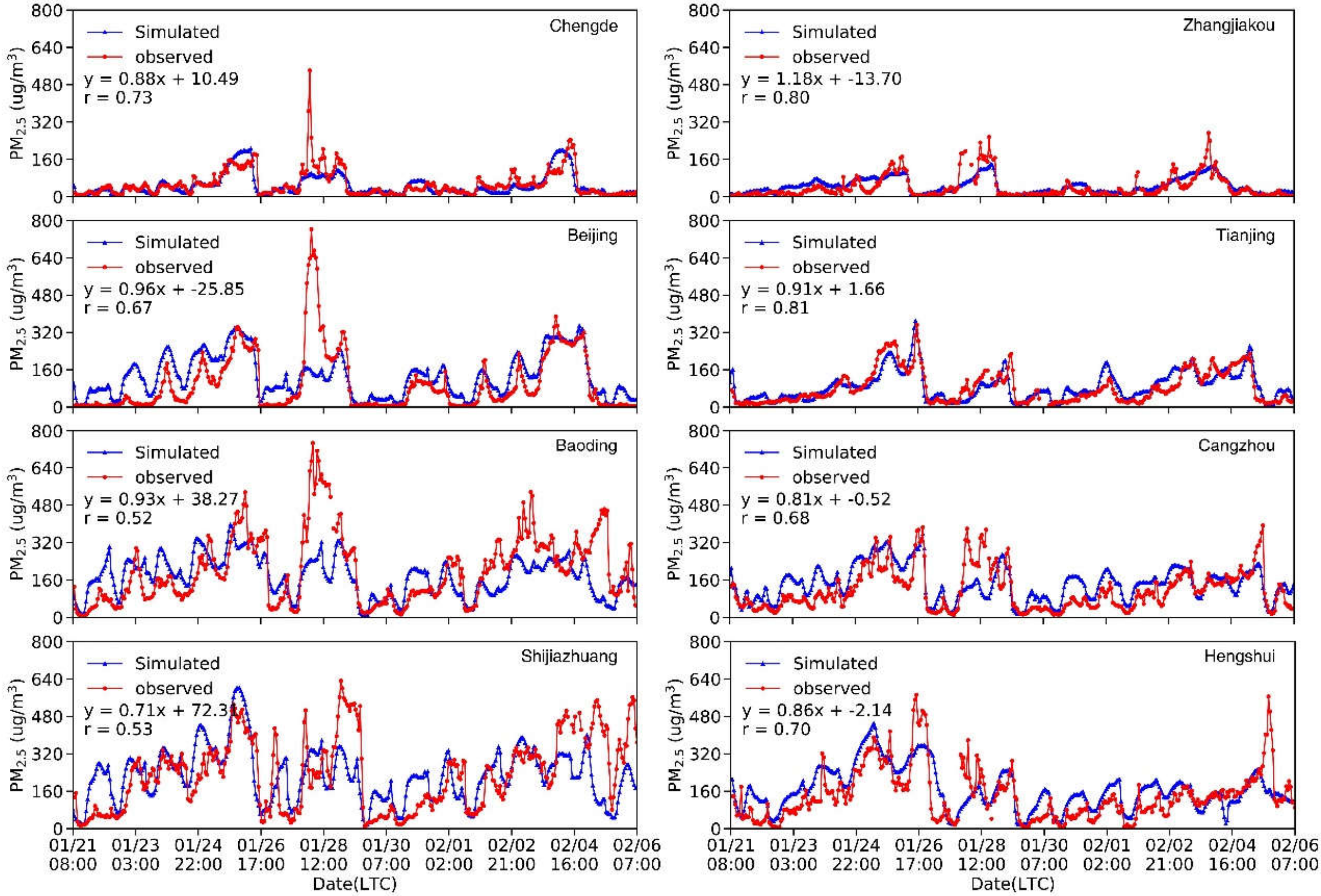

Figure S5. Comparison of simulated and observed $PM_{2.5}$ during the whole observation. Time series of the observed (red dots) and simulated (blue triangle) hourly $PM_{2.5}$ concentrations (μg/m^3) in the eight cities (Chengde, Zhangjiakou, Beijing, Tianjing, Baoding, Cangzhou, Shijiazhuang and Hengshui) from 21 Jan to 6 Feb 2017.

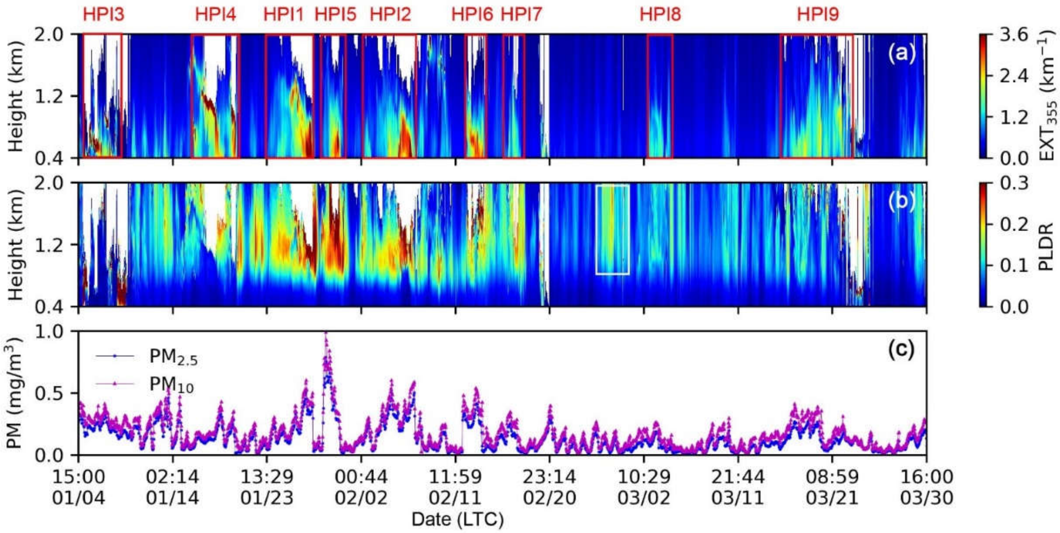

Figure S6. Periodic air pollution cycles during our whole observation. The color contours show the vertical structure of (**a**) EXT_{355} and (**b**) PLDR. (**c**) Temporal evolutions of surface average $PM_{2.5}$ and PM_{10} mass concentrations observed by six environmental monitoring stations in Baoding. Each HPI is marked with a red rectangle in (**a**), and the HPI number is displayed on the top of each red rectangle. The detailed date of each HPI is listed in Table S1.

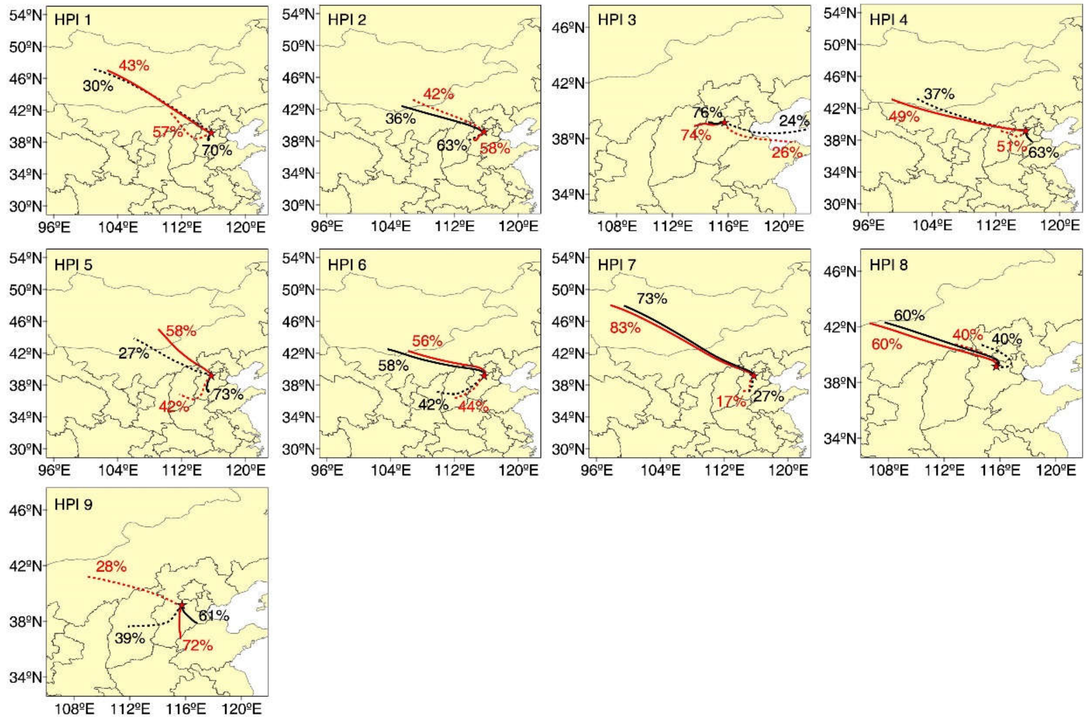

Figure S7. Cluster analysis of 24–h air mass backward trajectories (AMBTs) initialized at 500 m (black) and 1000 m (red) during each HPI. The numbers in the map are the fraction of each category of AMBTs. The 24–hour AMBTs were computed using the Hybrid Single–Particle Lagrangian Integrated Trajectory (HYSPLIT) model of the National Oceanic and Atmospheric Administration (Draxler and Hess, 1998). We calculated the hourly AMBTs during the whole observation period initialized at 500 m and 1000 m. Then, cluster analysis of AMBTs was conducted in two categories directions. The HPI number is shown in top left of each panel.

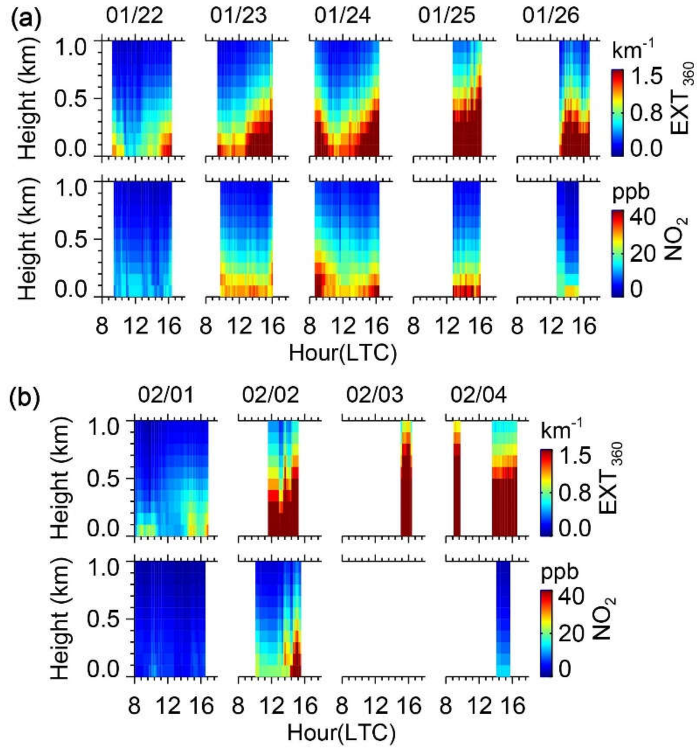

Figure S8. Curtain plots of MAX–DOAS observations. (**a**) EXT_{360} and NO_2 VMR from 22 to 26 Jan 2017, (**b**) EXT_{360} and NO_2 VMR from 1 to 4 Feb 2017.

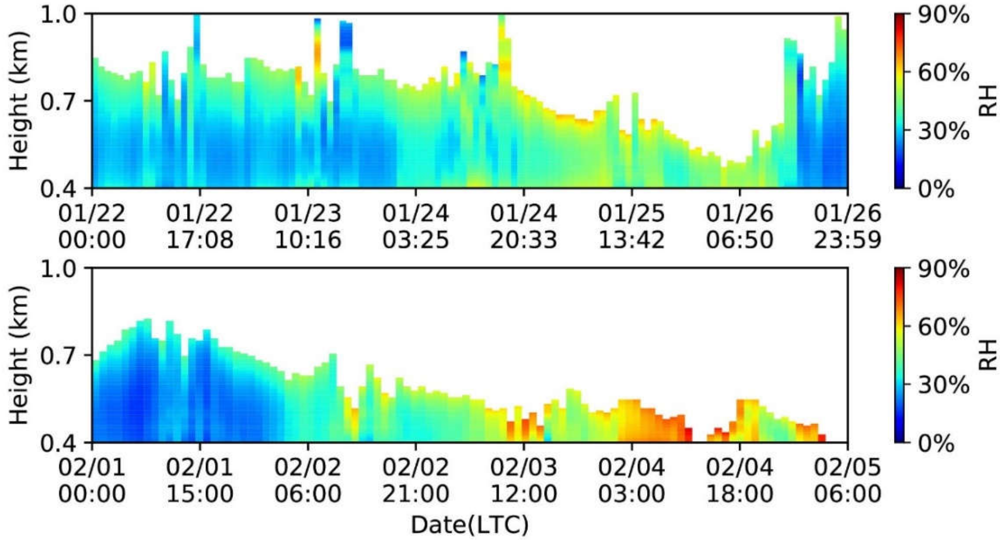

Figure S9. Curtain plots of relative humidity during HPI 1 and HPI 2.

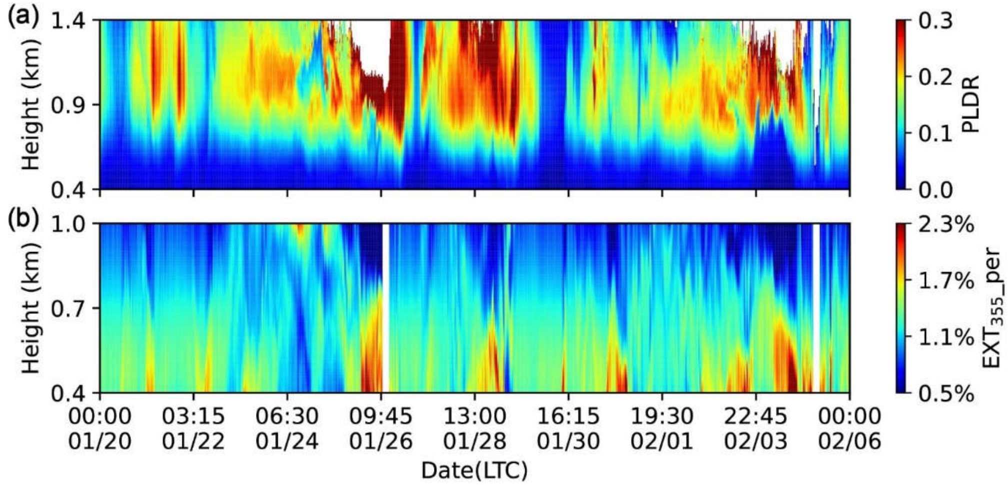

Figure S10. Correlation between PLDR and EXT_{355} from 20 Jan to 5 Feb 2017. The vertical structure of (**a**) PLDR, and (**b**) percentage of EXT_{355} of total EXT_{355}. The percentage of EXT_{355} is used to characterize the aerosol concentrations at different heights, which is defined as: $EXT_{355\_per}(z) = 100\% \times EXT_{355}(z)/\sum_{z=400}^{1000} EXT_{355}(z)$. Where EXT_{355_per} is the percentage of EXT_{355}, z is the height.

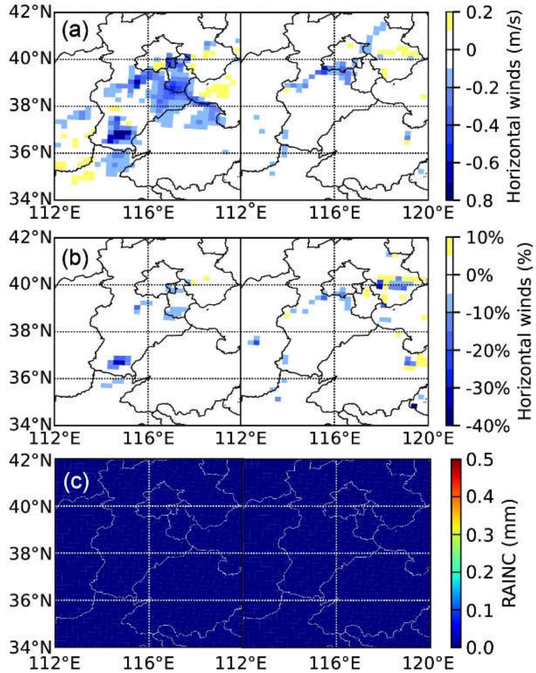

Figure S11. Influence of elevated dust on surface winds in HPI 1 and HPI 2 dissipation stages. (a) Difference in surface horizontal winds between the experiments dust_on and dust_off. (b) Percentage change in surface horizontal winds between the experiments dust_on and dust_off. The time of each subgraph is the HPI 1 dissipation stage at 13:00 LT on 26 Jan 2017 (left panel) and HPI 2 dissipation stage at 16:00 LT on 4 Feb 2017 (right panel). (c) Mean convective precipitation (RAINC) between two experiments dust_on (left) and dust_off (right) in WRF-Chem simulations from 20 Jan to 4 Feb 2017

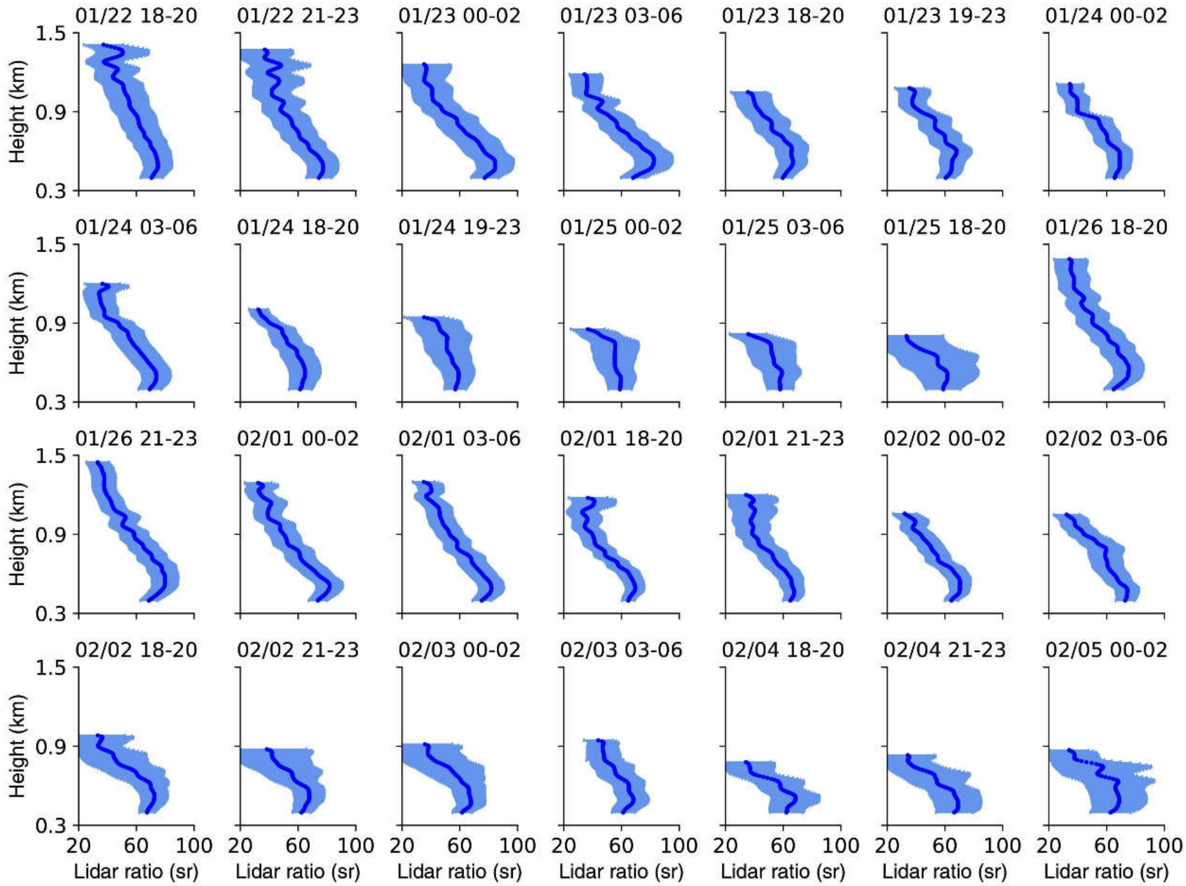

Figure S12. Lidar ratio profiles at 355 nm measured during HPI 1 and HPI 2. Three–hour average LR profile is the thick blue line and the envelope represents the errors at each altitude. The time (LTC) of each profile is displayed at the top of each panel. Error bars are calculated from the law of error propagation, which primarily depends on the signal–to–noise ratio (Heese et al., 2010) of the input signal given in Table 1.

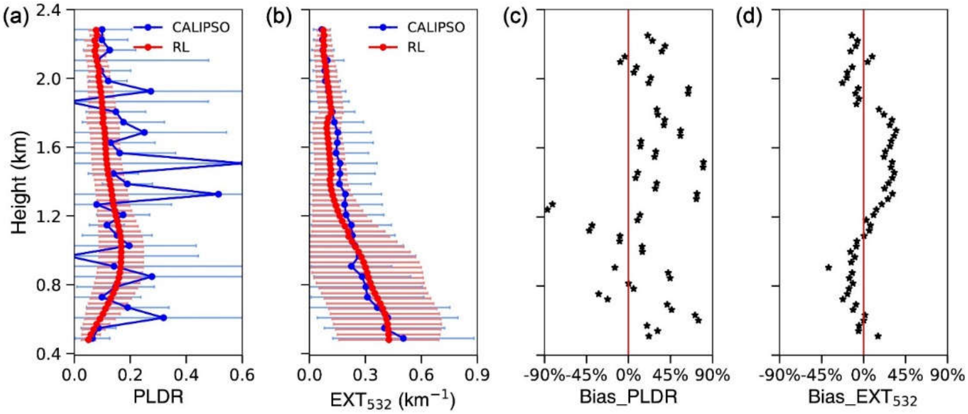

Figure S13. Comparison of average PLDR and EXT_{532} between RL and CALIPSO over Jan to Mar 2017. (**a**) Comparison of PLDR, and (**b**) EXT_{532} measured by CALIPSO and RL. The envelope over the horizontal bars in (**a**) and (**b**) represents one standard deviation at each altitude. The relative bias of PLDR and EXT_{532} compared with RL and CALIPSO are shown in (**c**) and (**d**), respectively.

Table S1. The duration of each HPI during our whole observation.

Case	Period (LTC)
HPI 1	2017/01/22 11:00–2017/01/26 23:00
HPI 2	2017/02/01 11:00–2017/02/05 06:00
HPI 3	2017/01/05 04:00–2017/01/08 04:00
HPI 4	2017/01/15 10:00–2017/01/19 12:00
HPI 5	2017/01/27 14:00–2017/01/29 07:00
HPI 6	2017/02/14 16:00–2017/02/16 13:00
HPI 7	2017/02/18 00:00–2017/02/19 18:00
HPI 8	2017/03/03 10:00–2017/03/05 20:00
HPI 9	2017/03/16 03:00–2017/03/23 05:00

Table S2. CALIPSO overpasses (within 150 km distance) used for comparison during our observation period.

Date	Time (UTC)	Separation (km)
23 Jan	1813	51
1 Feb	1808	83
2 Feb	0448	144
8 Feb	1815	51
9 Feb	0454	14
17 Feb	1809	83
18 Feb	0449	144
24 Feb	1816	53
25 Feb	0456	13
5 Mar	1811	83
6 Mar	0451	144
12 Mar	1838	49
21 Mar	1813	88
28 Mar	1820	46
29 Mar	0500	8